Monthly Notices of the ROYAL ASTRONOMICAL SOCIETY

MNRAS **464,** 2854–2865 (2017) doi:10.1093/mnras/stw2562
Advance Access publication 2016 October 6

Fast evolving pair-instability supernova models: evolution, explosion, light curves

Alexandra Kozyreva,[1,2]★ Matthew Gilmer,[3] Raphael Hirschi,[2,4] Carla Fröhlich,[3] Sergey Blinnikov,[4,5,6] Ryan T. Wollaeger,[7] Ulrich M. Noebauer,[8] Daniel R. van Rossum,[9] Alexander Heger,[10,11,12] Wesley P. Even,[7] Roni Waldman,[13] Alexey Tolstov,[4] Emmanouil Chatzopoulos[14] and Elena Sorokina[4,5,15]

[1]*The Raymond and Beverly Sackler School of Physics and Astronomy, Tel Aviv University, Tel Aviv 69978, Israel*
[2]*Astrophysics group, Keele University, Keele, Staffordshire ST5 5BG, UK*
[3]*Department of Physics, North Carolina State University, Raleigh, NC 27695-8202, USA*
[4]*Kavli Institute for the Physics and Mathematics of the Universe (WPI), Tokyo Institutes for Advanced Study, The University of Tokyo, 5-1-5 Kashiwanoha, Kashiwa, Chiba 277-8583, Japan*
[5]*ITEP (Kurchatov Institute), Moscow 117218, Russia*
[6]*VNIIA, Moscow 127055, Russia*
[7]*Center for Theoretical Astrophysics/CCS-2, Los Alamos National Laboratory, Los Alamos, NM 87544, USA*
[8]*Max-Planck-Institut für Astrophysik, Karl-Schwarzschild-Straβe 1, D-85748 Garching, Germany*
[9]*Flash Center for Computational Science, University of Chicago, Chicago, IL 60637, USA*
[10]*Monash Centre for Astrophysics, School of Physics and Astronomy, Monash University, VIC 3800, Australia*
[11]*Center for Nuclear Astrophysics, Department of Physics and Astronomy, Shanghai Jiao-Tong University, Shanghai 200240, China*
[12]*School of Physics and Astronomy, University of Minnesota, Minneapolis, MN 55455, USA*
[13]*Racah Institute of Physics, The Hebrew University, Jerusalem 91904, Israel*
[14]*Department of Physics and Astronomy, Louisiana State University, Baton Rouge, LA 70803-4001, USA*
[15]*Sternberg Astronomical Institute, M.V. Lomonosov Moscow State University, Moscow 119991, Russia*

Accepted 2016 October 5. Received 2016 October 4; in original form 2016 March 7; Editorial Decision 2016 October 4

ABSTRACT

With an increasing number of superluminous supernovae (SLSNe) discovered, the question of their origin remains open and causes heated debates in the supernova community. Currently, there are three proposed mechanisms for SLSNe: (1) pair-instability supernovae (PISNe), (2) magnetar-driven supernovae and (3) models in which the supernova ejecta interacts with a circumstellar material ejected before the explosion. Based on current observations of SLSNe, the PISN origin has been disfavoured for a number of reasons. Many PISN models provide overly broad light curves and too reddened spectra, because of massive ejecta and a high amount of nickel. In the current study, we re-examine PISN properties using progenitor models computed with the GENEC code. We calculate supernova explosions with FLASH and light-curve evolution with the radiation hydrodynamics code STELLA. We find that high-mass models (200 and 250 $M_{\odot}$) at relatively high metallicity ($Z = 0.001$) do not retain hydrogen in the outer layers and produce relatively fast evolving PISNe Type I and might be suitable to explain some SLSNe. We also investigate uncertainties in light-curve modelling due to codes, opacities, the nickel-bubble effect and progenitor structure and composition.

Key words: radiative transfer – stars: evolution – stars: massive – supernovae: general – supernovae: individual: PTF12dam.

1 INTRODUCTION

The evolution of very massive stars[1] at zero metallicity, i.e. without mass-loss, with initial mass between approximately 140 and

[1] According to the analysis and definition by Bond, Arnett & Carr (1982) and Carr, Bond & Arnett (1984), a very massive star is a star with initial mass above approximately 100 $M_{\odot}$ and below several 10^4 $M_{\odot}$.

★ E-mail: a.kozyreva@keele.ac.uk

260 $M_\odot$, is more or less clear. Following the sequence of hydrostatic hydrogen, helium, carbon and neon burning, the hydrodynamical instability develops due to electron–positron pair creation caused by dominating radiation pressure (Barkat, Rakavy & Sack 1967; Bisnovatyi-Kogan & Kazhdan 1967; Rakavy & Shaviv 1967; Fraley 1968, and others). Subsequently, oxygen and silicon burn explosively. If the nuclear burning energy released exceeds the binding energy of the star, the star blows up in an explosion – a pair-instability supernova (hereafter PISN). The amount of radioactive nickel generated during the explosion phase may be as high as 55 $M_\odot$ (Heger & Woosley 2002) resulting in a very bright supernova event. Nevertheless, the major uncertainties in the evolution of very massive stars are the mass-loss prescriptions and the treatment of convection (Vink 2015; Woosley & Heger 2015).

Observationally, astrophysicists have clear confirmation of the existence of very massive stars in nearby galaxies (see e.g. Crowther et al. 2010; Schneider et al. 2014). In fact, it is hard to measure the mass of an individual star, as many massive stars are born in tight clusters (Lada & Lada 2003; Zinnecker & Yorke 2007, see also discussion in Habibi, Stolte & Harfst 2014). With the approaching launch of the *James Webb Space Telescope*, it will still be difficult to resolve individual stars (Rydberg et al. 2013). Even if it is difficult to catch glimpse of these rare very massive stars, their powerful explosions, i.e. supernovae, may be detectable up to very high redshifts (Whalen et al. 2013a). Fitting the supernova observations with the theoretical simulations primarily helps in understanding the evolution and explosion of these very massive star populations.

Modern large survey telescopes lead to the detection of hundreds of supernovae each year (Gal-Yam et al. 2013). A small fraction of these supernovae reach a significantly higher peak luminosity than an average supernova (Leaman et al. 2011; Li et al. 2011; Quimby et al. 2011; Gal-Yam 2012; Nicholl et al. 2014; Richardson et al. 2014). One of the possible mechanisms for these superluminous explosions is PISNe powered by radioactive nickel decay.

Recent studies clearly show that metal-free ($Z = 0$) or almost metal-free ($Z = 10^{-4}\,Z_\odot$) PISN models retain a very massive hydrogen-rich envelope because of an absence of mass-loss or a very low mass-loss rate (Kasen, Woosley & Heger 2011; Dessart et al. 2013). There is a large uncertainty because mass-loss rates at low metallicity are extrapolated from rates derived for considerably higher metallicity (Hirschi 2007; Vink 2015). These metal-free progenitors originate in a low-metallicity environment, i.e. in the early Universe (Scannapieco et al. 2005; Pan, Kasen & Loeb 2012; Whalen et al. 2013b). As a consequence, these massive PISNe display very broad light curves (Kasen et al. 2011; Dessart et al. 2013). The large amount of radioactive nickel powers the light curve at maximum and makes it brighter and broader for higher nickel mass (Kozyreva et al. 2016). Even assuming a hydrogen-free ejecta, the resulting light curves are still too broad to be considered viable candidates for most superluminous supernovae (SLSNe; Kasen et al. 2011; Chatzopoulos et al. 2015). A hydrogen-free PISN progenitor may originate from the evolution of a hydrogen-rich star which lost its hydrogen during hydrogen and helium core burning via stellar winds, pulsations or binary interactions (Baraffe, Heger & Woosley 2001). In addition, a number of studies show that their spectra are too red, both at earlier times (Dessart et al. 2012, 2013; Chatzopoulos et al. 2015) and during the nebular phase (Jerkstrand, Smartt & Heger 2016b); this makes PISNe with or without hydrogen inadequate for explaining blue SLSN spectra (Nicholl et al. 2014, 2015).

The situation is different for PISN progenitors at higher metallicity, $Z \sim 0.001$. If stars retain hydrogen in their atmosphere, the light curves are still broad, but not as broad as their metal-free siblings (Kozyreva et al. 2014). Therefore, they are good candidates for explaining at least some slowly evolving SLSNe like SN 2007bi. Although the colour temperatures for these PISNe hardly matche the majority of SLSNe, they are reasonably close to the colour temperatures for slowly evolving SLSNe. It may happen that very massive stars at non-zero metallicity ($Z = 10^{-3}$ to $Z = 2 \times 10^{-3}$, and higher, up to the PISN metallicity threshold $Z = 6 \times 10^{-3}$) never retain hydrogen (Yusof et al. 2013; Hirschi 2015). The stellar evolution simulations show that stars quickly lose their hydrogen atmosphere and in the most extreme cases also lose most of their helium layer, leaving a 2–3 $M_\odot$ shallow helium envelope. This is mainly caused by the mass-loss rate which is higher for higher metallicity (see Yusof et al. 2013, for more details). Because of the low helium abundance and absence of hydrogen, nothing prevents the recombination front from rapidly moving through the outer layers and reach the cloud of diffusing photons produced by the decay of the nickel and cobalt. These very massive stars might result in a faster evolving PISN.

In this study, we consider calculations for PISN progenitors which lost all hydrogen and a large fraction of helium. We analyse our numerical results in the context of the SLSN PTF12dam.

We describe our models in Section 2, present the resulting light curves and photospheric evolution in Section 3. In Section 4, we discuss the results in the context of SLSNe. Comparative analysis is done in Section 5. We conclude our study in Section 6.

2 INPUT MODELS AND LIGHT-CURVE MODELLING

2.1 Stellar evolution models

Our main input models are the following: non-rotating 200 and 250 $M_\odot$ stars at metallicity $Z = 10^{-3}$ (hereafter P200 and P250, see Table 1). The evolution during hydrogen, helium, carbon core burning is computed with the stellar evolution code GENEC (Ekström et al. 2012; Yusof et al. 2013). The details of the physical ingredients of the models are as described by Ekström et al. (2012). We list the main features here.

(i) The initial abundances for these models are adapted from Asplund, Grevesse & Sauval (2005) except for the neon abundances adopted from Cunha, Hubeny & Lanz (2006), considering enhanced α-element abundances and a total metallicity, $Z = 10^{-3}$.

(ii) Nuclear reaction rates are generated by NetGen tools where they take most of the data from NACRE (Angulo et al. 1999). The current NACRE data have been redetermined and updated, and some of the comparison to NACRE values and a short description of the effects on stellar evolution have been described in Ekström et al. (2012).

(iii) Neutrino energy loss in plasma, including pair and photoneutrino processes, is taken from Itoh et al. (1989) and Itoh et al. (1996).

(iv) Opacity is taken from OPAL (Iglesias & Rogers 1996) and complemented with low temperature opacities from Ferguson et al. (2005) adapted for the high neon abundance.

(v) The convective core is extended with an overshoot parameter $d_{\rm over}/H_{\rm P} = 0.10$ starting from the Schwarzschild limit.

(vi) Since models calculated are $>100\,M_\odot$, the outer convective zone is treated according to mixing length theory, using $\alpha_{\rm MLT} = 1.0$. This is because, for the most luminous models, the turbulent pressure and acoustic flux need to be included in the treatment of the

Table 1. Characteristics of the PISN models. All masses are in solar masses (H for hydrogen, He for helium, CO core for the carbon–oxygen core, defined as the mass coordinate where $X_C + X_O = 0.5$, ^{56}Ni for radioactive nickel). For helium, the numbers in parentheses stand for helium mass only in the outer layers. E_{kin} is the kinetic energy at infinity in Bethe (B), i.e. in 10^{51} erg. $M_{above\,Ni}$ stands for mass above the region containing ^{56}Ni, i.e. the shell where ^{56}Ni mass fraction turns below 10^{-4}. v_{Ni} stands for the velocity of this shell. We include the helium PISN model He130 (Kasen et al. 2011) and the hydrogen-rich PISN model 250M (Kozyreva et al. 2014) for comparison.

Model name	M_{fin} ($M_\odot$)	Z	R ($R_\odot$)	H ($M_\odot$)	H surf	He ($M_\odot$)	He surf	CO core ($M_\odot$)	^{56}Ni ($M_\odot$)	$M_{above\,Ni}$ ($M_\odot$)	v_{Ni} (1000 km s^{-1})	E_{kin} (B)
P200	110	0.001	81	0.01	0.05	9	0.94	100	12	95	3.2	53
P250	127	0.001	2	0	0	2.6(2)	0.34	116	34	49	7.5	86
He130	130	0	7	0	0	2.8(1.65)	1	121	40	64	8	90
250M	169	0.001	745	10	0.27	48	0.72	110	19	115	5.3	48

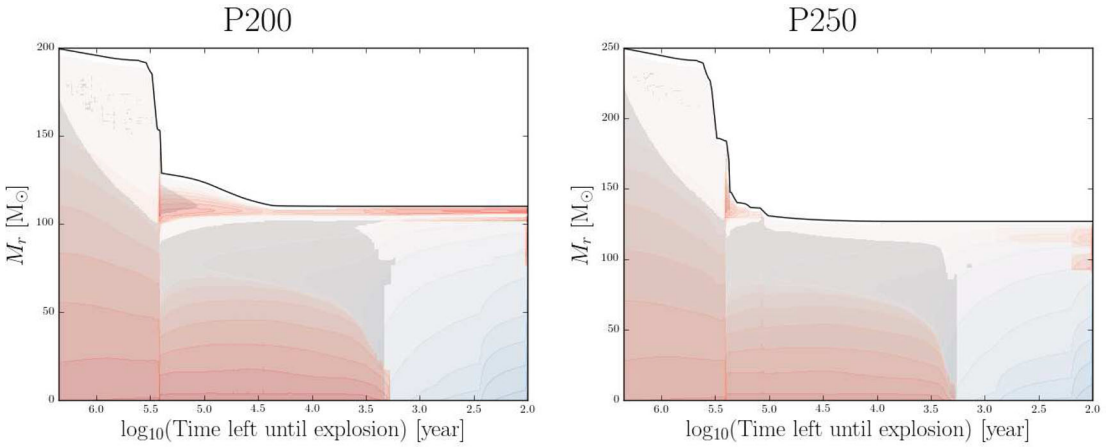

Figure 1. Structure evolution (aka Kippenhahn) diagrams for the 200 $M_\odot$ (P200, left) and 250 $M_\odot$ (P250, right) as a function of age. The grey zones represent the convective regions. The top solid line corresponds to the total mass. Reddish area indicates the regions where energy is released via nuclear burning, and bluish area indicates cooling via neutrino losses.

envelope. The choice of outer convective zone for different initial mass has been described in detail in Ekström et al. (2012).

(vii) We adopted mass-loss for hot O stars from Vink, de Koter & Lamers (2001). When the models reach the Wolf–Rayet (WR) transition, i.e. hydrogen surface abundance drops below 0.3, we adopted the mass-loss rate of WR from Nugis & Lamers (2000) or Gräfener & Hamann (2008) depending on which effective temperature is reached by the models. For the temperature domains not covered by Vink et al. (2001) and Nugis & Lamers (2000) or Gräfener & Hamann (2008), the mass-loss prescription from de Jager, Nieuwenhuijzen & van der Hucht (1988) is used.

The evolution of the two models is shown in Fig. 1. Both models experience strong mass-loss both just before and just after the main sequence. This is due to the models reaching low enough temperatures to first reach the bistability limit (Vink et al. 2001) and then the limit of the domain of validity of the Vink et al. (2001) prescriptions. At this point, the code switches to the de Jager et al. (1988) mass-loss, which is an uncertain empirical prescription including strong mass-loss linked to the luminous variable phase (Glatzel & Kiriakidis 1993; Humphreys & Davidson 1994). After most of the hydrogen-rich envelope is lost, the surface layers contract and the models enter the WR phase, during which mass-loss rates become relatively modest at $Z = 10^{-3}$ (around 10^{-4} $M_\odot$ yr^{-1} as opposed to up to $10^{-2.5}$ $M_\odot$ yr^{-1} during the Luminous blue variable phase). While model P200 retains a small amount of hydrogen near its surface (0.05 $M_\odot$), model P250 loses all of its hydrogen and most of its helium.

2.2 Pair-instability explosion

Near the end of carbon burning, a fraction of the oxygen core undergoes a dynamical instability as dominating radiation pressure allows the production of electron–positron pairs. Even though the equations of state of both radiation-dominated plasma and a mixture of plasma+radiation+pairs have an adiabatic index close to 4/3 ($P \sim \rho^{4/3}$), there is an offset between them. The *phase transition* between 'radiation' and 'radiation+pairs' thus causes the effective adiabatic index to drop below its equilibrium value of 4/3 (see fig. 32 on page 237 in Zeldovich & Novikov 1971; Zel'dovich, Blinnikov & Shakura 1981; Blinnikov, Dunina-Barkovskaya & Nadyozhin 1996). However, GENEC is not capable of following this instability, because the equation of state implemented into GENEC does not include electron–positron pair pressure. Therefore, models were mapped into the hydrodynamical code FLASH[2] at this evolutionary stage (version 4.3; Fryxell et al. 2000; Dubey et al. 2009; Chatzopoulos, Wheeler & Couch 2013b; Chatzopoulos et al. 2015). For the FLASH simulations, we used the Helmholtz equation of state (Timmes & Swesty 2000) which includes pressure contributions from electron–positron pairs. The nuclear burning is calculated according to the 19-isotope reaction network Aprox19,[3] which includes α-chain and heavy-ion reactions as well as photodisintegration and nucleon captures between the isotopes, ^{52}Fe, ^{54}Fe and ^{56}Ni.

[2] http://flash.uchicago.edu/site/flashcode/
[3] http://cococubed.asu.edu/code_pages/net_torch.shtml

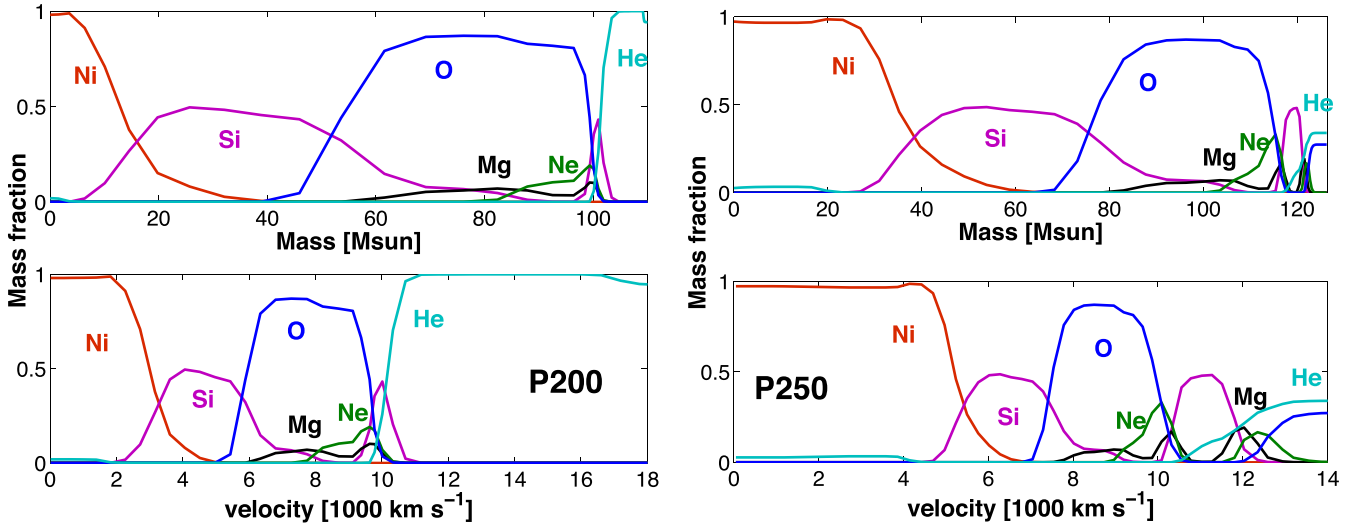

Figure 2. Chemical structure of the 200 $M_\odot$ (P200, left) and 250 $M_\odot$ (P250, right) non-rotating PISN models simulated with FLASH after the pair-instability explosion and when all nuclear burning is over. Top: versus mass coordinate. Bottom: versus radial velocity of the ejecta (in 1000 km s^{-1}).

The energy generation rates are calculated from the derivatives of abundances. This allows us to calculate the explosive nuclear burning coupled with hydrodynamics. The nuclear time-scale becomes comparable to the dynamical time-scale at the end of neon core burning and throughout the explosive phase.

All of our FLASH simulations were carried out in spherical symmetry with the new directionally unsplit hydrodynamics solver (Lee, Deane & Federrath 2009) using the third-order piece-wise parabolic method (Colella & Woodward 1984; Woodward & Colella 1984; Fryxell, Müller & Arnett 1989). For both our models, the core (within 5×10^{10} cm for P250 or within 4.167×10^{10} cm for P200) was mapped first into FLASH and evolved through collapse to the onset of explosion, and until all nuclear burning was completed. The initial envelope was then appended on to the exploding core and mapped back into FLASH to follow shock burning up until the moment before shock breakout. To achieve convergence in the explosion properties with resolution, we performed a series of simulations varying the maximum refinement level as well as the refinement criteria, while the minimum resolution remained constant at 4.4×10^8 cm. The maximum resolution ranged from 1.1×10^8 to 6.9×10^6 cm, and the refinement criteria were modified in order to allow the various maximum refinement levels to be reached in the central regions during the explosive burning phase. Variations in the total nickel-56 yield for the above range of maximum resolutions were at the 17 per cent level. The simulations presented here used a maximum refinement of 6.5×10^7 cm and produced 12 and 34 $M_\odot$ of nickel-56 for models P200 and P250, respectively. We will present details of the FLASH simulations in the forthcoming paper (Gilmer et al., in preparation). The collapse phase and explosion phase are computed without any special non-physical assumptions. The collapse is caused naturally by a hydrodynamical instability, since FLASH properly treats the inclusion of pairs in the equation of state. The explosion is driven by the energy deposition from oxygen and silicon nuclear burning followed by the FLASH nuclear network.

In Fig. 2, we present the chemical structure of the models as they were mapped into the STELLA code for calculating further hydrodynamical and radiative evolution. We plot the most influential and abundant species – helium, oxygen, neon, magnesium, silicon and nickel-56. The effects of the shock initiated nucleosynthesis can be seen in the dips at the oxygen–helium interfaces where shock heating has triggered α-captures on carbon and oxygen producing silicon. Mass fractions at the surface of the model P250 are roughly: carbon – 0.39, helium – 0.34 and oxygen – 0.27 – resulting from convective helium shell burning. The envelope above this layer was completely lost due to the stellar wind during earlier evolutionary phases (Yusof et al. 2013). We list the properties of our progenitor models and the explosion results in Table 1.

2.3 Post-explosion dynamics with STELLA

To simulate the supernova ejecta evolution and the light curves, we used the one-dimensional radiation hydrodynamics code STELLA (Blinnikov et al. 2006; Kozyreva et al. 2014). The PISN models are mapped into STELLA before the shock reaches the surface of the progenitor, i.e. just before shock breakout. While mapping into STELLA, P200 and P250 models were divided into 194 and 116 zones, respectively.

STELLA solves the radiative transfer equations in the intensity momentum approximation in each frequency bin. We use 100 frequency groups in the current study. These are enough groups to produce spectral energy distribution, but are not sufficient to produce spectra. The opacity is computed based on about 153 441 spectral lines from Kurucz & Bell (1995) and Verner, Verner & Ferland (1996). The expansion opacity formalism from Eastman & Pinto (1993) is used for line opacity taking the effect of high velocity gradients into account. Opacity also includes photoionization, free–free absorption and electron scattering. Local thermodynamic equilibrium (LTE) is assumed in the plasma, which allows the use of the Boltzmann–Saha distribution for ionization and level populations. STELLA does not include a nuclear network except radioactive decay of nickel-56 to cobalt-56, and to iron-56. The code uses 16 species for calculating the overall opacity. These are H, He, C, N, O, Ne, Na, Mg, Al, Si, S, Ar, Ca, a sum of stable Fe and radioactive ^{56}Co, stable Ni and radioactive ^{56}Ni. Energy from nickel and cobalt radioactive decay is deposited into positrons and gamma-photons and is treated in a one-group transport approximation according to Swartz, Sutherland & Harkness (1995).

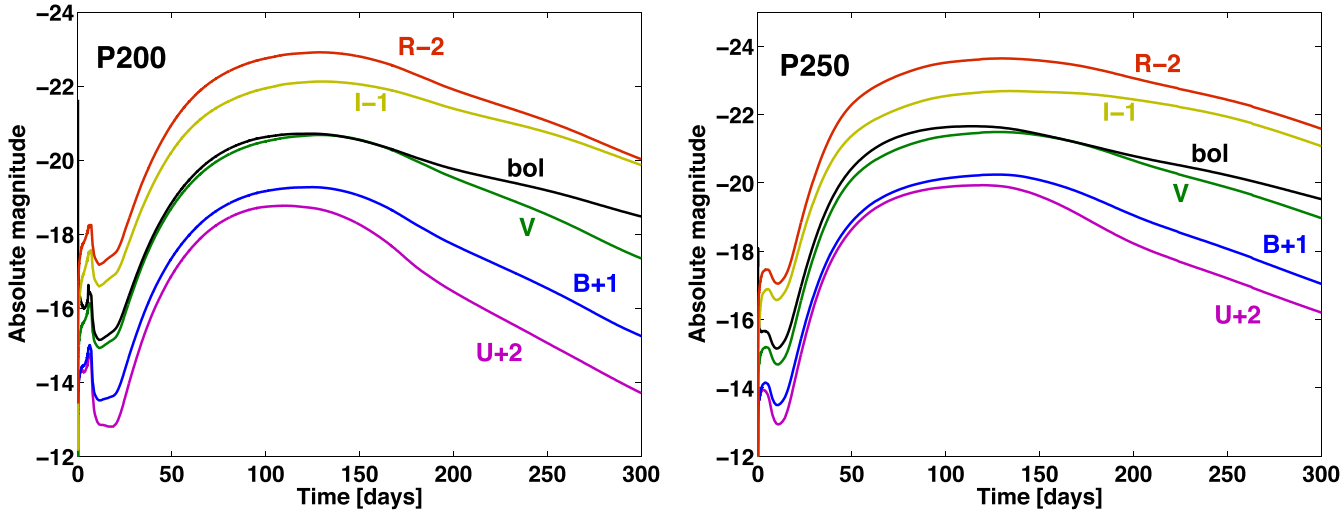

Figure 3. 200 $M_\odot$ (left: P200) and 250 $M_\odot$ (right: P25) PISN bolometric (black) and *UBVRI* broad-band light curves.

STELLA solves the conservation equations for mass, momentum and total energy in the Lagrangian comoving grid. The artificial viscosity consists of the standard von Neumann artificial viscous pressure used for stabilizing solution (von Neumann & Richtmyer 1950) and a so-called cold artificial viscosity used to smear shocks (Blinnikov et al. 1998; Moriya 2013). Therefore, STELLA allows one to properly compute the propagation of the shock along the ejecta and the shock breakout event. The coupled equations of radiation hydrodynamics (system of ordinary differential equations) are solved through an implicit high-order predictor–corrector procedure based on the methods of Gear (1971) and Brayton, Gustavson & Hatchel (1972, see details in Blinnikov & Panov 1996; Stabrowski 1997). The required accuracy is set at the level of 10^{-3}–10^{-4}, whereas the actual accuracy is better than 1 per cent.

STELLA was successfully applied to normal and peculiar SNe Ia (Sorokina, Blinnikov & Bartunov 2000; Blinnikov et al. 2006; Phillips et al. 2007), SNe IIP (Baklanov, Blinnikov & Pavlyuk 2005; Tolstov et al. 2016b), SNe IIpec (SN 1987A, SN 1993J; Blinnikov et al. 1998, 2000) and SNe IIL (Blinnikov & Bartunov 1993; Moriya et al. 2016). Since STELLA is a hydrodynamics code, it is widely used for simulations of interacting supernovae, in which normal supernova ejecta collide with a shell or dense circumstellar environment or a wind (Moriya et al. 2011; Baklanov, Sorokina & Blinnikov 2015; Sorokina et al. 2016). Kozyreva et al. (2014) use STELLA for simulating post-explosion radiation and hydrodynamical evolution of low-mass and high-mass hydrogen-rich PISNe.

In some of our simulations, the outermost layers of the supernova ejecta reach very high velocities. In these cases, we truncated a small fraction of the outer layer, to ensure stability of the STELLA simulations. This causes a slightly weaker luminosity (since $L \sim R^2$) at the so-called plateau phase before re-brightening, but does not affect the main nickel-powered maximum, because the layer removed is almost massless and does not carry much kinetic energy.

3 RESULTS

We show the bolometric and broad-band light curves for our main models P200 and P250 in Fig. 3. P200 and P250 reach a maximum bolometric luminosity of 6×10^{43} and 1.4×10^{44} erg s^{-1}, respectively. All figures start with time '0' which corresponds to the time at the beginning of the STELLA simulations.

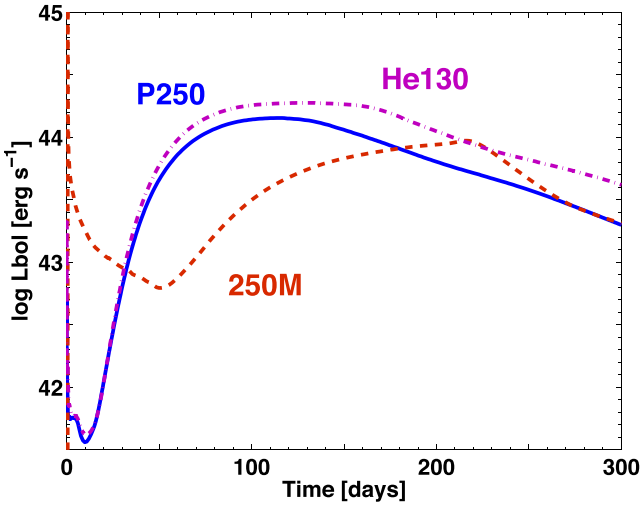

Figure 4. Bolometric light curves for the model P250 (solid), helium He130 (dash–dotted) and the hydrogen-rich PISN model 250M (dashed; Kozyreva et al. 2014). All light curves are calculated with STELLA.

We mapped the FLASH P200 and P250 outputs into STELLA, when the shock propagates through the outer layer. The shock reaches the surface during time $\approx R/v_{\rm sound}$, i.e. almost immediately after mapping. According to Tolstov et al. (2016b), the duration of the shock breakout event mostly depends on the radius of the progenitor. In the case of our compact models, the shock breakout lasts about 9 min for P200 and 4 s for P250. Hence, in Fig. 3, the light curves begin with the shock breakout which remains unresolved on the plots because of relatively shorter time-scale.

One of the most noticeable features of the present results is the short rise time for the given PISN light curves. The re-brightening phase lasts about 100 d for both models, which is noticeably shorter than for previously published light curves. For instance, all models presented in Dessart et al. (2013) rise to maximum during about 150–200 d, and models presented in Kasen et al. (2011) rise during 150–400 d depending on the type of progenitor. In Fig. 4, we include the long-rising curve for the hydrogen-rich model 250M (Langer et al. 2007; Kozyreva et al. 2014) and helium model He130 (Kasen et al. 2011) together with the P250 curve for illustration. The

long rise time disfavours PISNe as a possible scenario to explain SLSNe. However, our new light curves of P200 and P250 PISNe evolve faster than hydrogen-rich PISNe and might be more relevant to at least some of the observed SLSNe. We explain the faster evolution of the P200 and P250 light curves by the very distinct distribution of hydrogen, helium and nickel-56 in the P200 and P250 models as explained below. It is well known that hydrogen is the most influential element supporting the electron-scattering opacity and governing the location of the photosphere. If hydrogen is absent, helium dominates the electron-scattering opacity. At the same time, the nickel-56 distribution also strongly impacts the light-curve appearance, especially during rise. The model 250M retains 58 $M_{\odot}$ of hydrogen–helium in the envelope which significantly impedes inward motion of the photosphere and delays re-brightening to the nickel-powered maximum for 200 d, while the P250 model has only 2 $M_{\odot}$ of helium in its atmosphere. The surface abundances in P250 are dominated by carbon and oxygen, with a mass fraction of 0.34 of helium. Radioactive material is distributed in up to half of the P250 ejecta by mass coordinate, and up to 30 per cent of the 250M ejecta. The combination of a small helium layer and closeness of radioactive material to the surface of the progenitor leads to a fast evolving light curve for the P250 model compared to the slowly evolving 250M model. Therefore, the 100 d rise time makes the new PISN models, presented in the current study, good candidates for explanation of some SLSNe.

The chemical structure of the model P250 resembles that of the model He130, although ^{56}Ni mass is higher in He130 than in P250, and surface helium mass fraction differs considerably. The higher ^{56}Ni mass leads to a broader peak, and the higher surface helium abundance in He130 causes a longer rise for the He130 light curve. Therefore, the P250 and He130 light curves differ. In Fig. 4, all light curves of 250M, P250 and He130 models are simulated with STELLA. The He130 light curve published earlier was computed with SEDONA (Kasen et al. 2011). The uncertainty of the results due to the different radiation codes will be discussed in Section 5.

The photosphere in our new models is located deep in the oxygen layer (close to the bottom of oxygen shell); therefore, P200 and P250 explosions appear as hydrogen- and helium-free at maximum light, i.e. as Type I supernovae. We discuss the applicability of the P200 and P250 models to SLSN PTF12dam in the next section.

4 COMPARISON TO SLSN PTF12DAM

Inspired by the short rise time of the P200 and P250 light curves and considerably high luminosity, we decided to put our models into the context of SLSNe. We choose SLSN PTF12dam as it is one of the well-observed recent SLSNe (Nicholl et al. 2013; Chen et al. 2015). In Fig. 5, we show the comparison of our models with the bolometric light curve of PTF12dam. The observed data are shifted by 100 d, allowing the observed peak luminosity to approximately coincide with the maximum of the P250 synthetic light curve. The figure demonstrates that the shape of the bolometric synthetic light curves resembles the behaviour of the observed light curve of PTF12dam around maximum epoch. Fig. 6 shows the synthetic curves of P200 and P250 in the *ugriz* bands and observed absolute *ugriz* magnitudes of PTF12dam.

Figs 7 and 8 show colour temperature and photospheric velocity evolution for the P200 and P250 models versus those of PTF12dam (Nicholl et al. 2013). We estimate the colour temperature based on the least-squares method using the spectral range from 1 to 50 000 Å. The colour temperature reaches 8100 K in the P200 model and 11 000 K in the P250 model at peak luminosity, which is higher

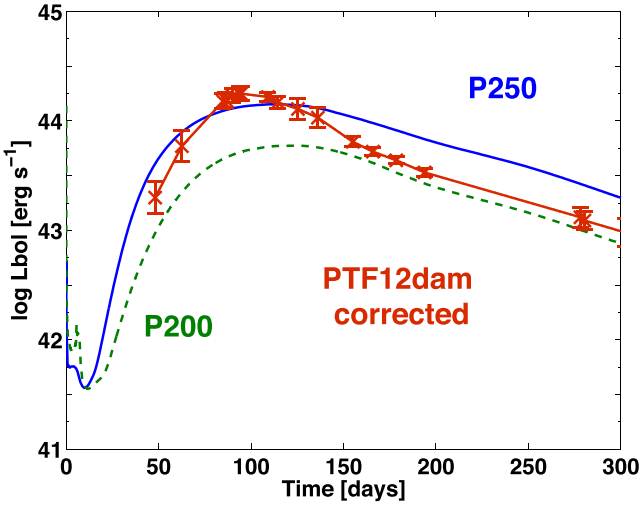

Figure 5. Bolometric light curves for the P200 and P250 PISN models and SLSN PTF12dam.

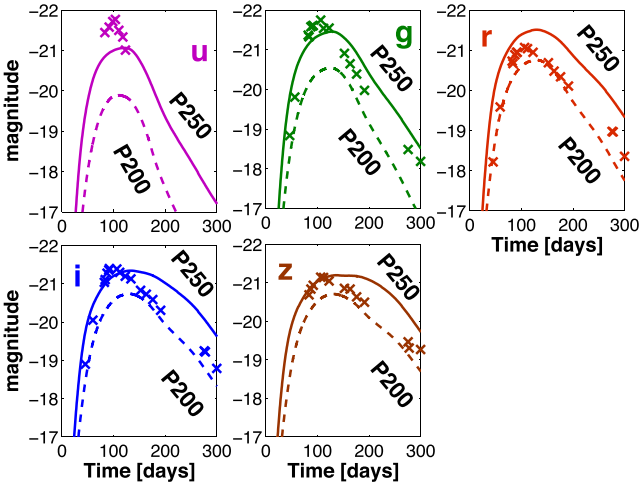

Figure 6. P200 (dashed) and P250 (solid) versus SLSN PTF12dam (crosses) in the *ugriz* bands.

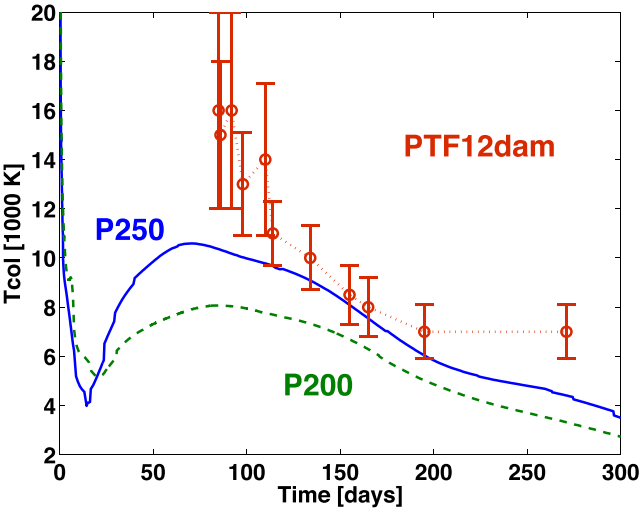

Figure 7. Colour temperature the P200 and P250 PISN models and that of SLSN PTF12dam.

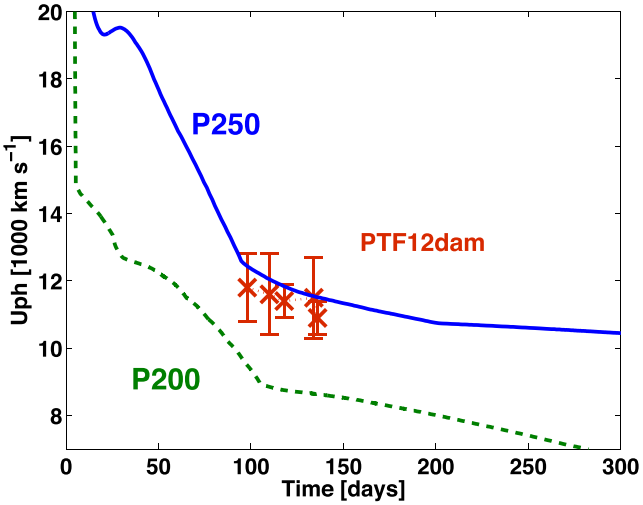

Figure 8. Photospheric velocity evolution for the P200 and P250 PISN models versus PTF12dam data.

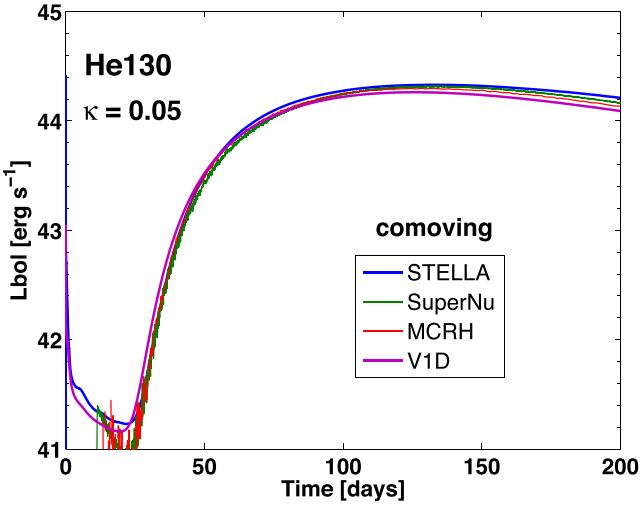

Figure 9. SUPERNU, STELLA, V1D and MCRH simulations of the He130 model with the constant opacity, $\kappa = 0.05$ in the comoving frame.

compared to previously published PISN models. The photospheric velocity is the radial velocity of the layer where the photosphere is located. The photospheric velocity is 9000 km s^{-1} (P200) and 12 000 km s^{-1} (P250) at peak luminosity, respectively.

P200 and P250 models reproduce parts of the PTF12dam data. In particular, P250 matches the earlier bolometric light curve to some degree, the peak luminosity, the colour temperature of P250 is close to the data points during 100 d after the bolometric peak, while photospheric velocity in P250 ejecta fully matches the observed velocity. P200 model better matches the late part of the light curve. Some features, however, are not well explained by the models. The colour temperature near the peak of the light curve is not matched by the models. The broad-band light curves also do not match very well, although this is difficult for any model to explain. We emphasize that our models are computed self-consistently and without fine tuning for PTF12dam. We conclude that the PISN scenario is still viable for PTF12dam.[4]

5 COMPARISON BETWEEN DIFFERENT NUMERICAL APPROACHES

As we show in Section 3, our new PISN models exhibit relatively short rise to the main nickel-powered maximum compared to previously published PISN light curves. In order to assess the robustness of these findings, we confront STELLA calculations to the results obtained with different numerical approaches used to solve the radiative transport problem in supernova ejecta. Here, we mainly focus on SEDONA which has been extensively used to predict PISN observables. All technical details of the different methods used in the following analysis are deferred to Appendix A.

5.1 The reference model: helium PISN He130

All calculations performed in this comparative analysis are based on the 130 $M_\odot$ helium PISN model He130 since it resembles our P250 PISN model fairly closely and since it is a well-accepted model in the PISN context. This model has been simulated with the KEPLER stellar evolution code (Weaver, Zimmerman & Woosley 1978; Woosley, Heger & Weaver 2002) from the helium main sequence, i.e. as a pure helium star without any wind mass-loss, through the pair-instability phase. It retains a shallow outer shell of 1.65 $M_\odot$ helium and produces 40 $M_\odot$ of radioactive nickel-56.

5.2 Simple test calculation

As a preparation, we avoid complications induced by different assumptions about ionization and excitation and by the details of the opacity treatments by construction a simple test problem based on the He130 model. In particular, we assume a constant, frequency-independent specific interaction cross-section ($\kappa = 0.05$ cm^2 g^{-1}) and run simulations with STELLA, V1D, and two Monte Carlo codes MCRH and SUPERNU (see description of the codes in Appendix A). The results are presented in Fig. 9 showing an excellent agreement between the bolometric light curves computed with all the different methods. Thus, when adopting the same physical assumptions, STELLA performs as well as other radiative transfer methods.

5.3 STELLA versus SEDONA

Having completed the first comparison under idealized conditions, we turn to calculations under more realistic conditions. In particular, we compute the evolution of the PISN model He130 with STELLA starting at 100 s after the pair-instability explosion (Heger & Woosley 2002). To avoid problems associated with relativistic effects, we truncate the initial KEPLER profile at about 10 per cent of speed of light. However, velocity exceeds this limit after the shock breaks out and reaches 5×10^9 cm s^{-1}. The obtained bolometric light curve is compared to the published SEDONA results in Fig. 10. The overall width and shape of the two light curves are in good agreement. If compared in detail, however, the bolometric light curve of He130 model seems to rise again faster when computed with STELLA. The difference amounts to approximately 50 d. When comparing the two calculations in different broad-bands, the discrepancies become a bit more noticeable as seen in Fig. 11. This is not too surprising given the differences in the detailed radiative transfer treatments (ionization and excitation prescriptions, opacity treatments, atomic data, etc.).

[4] The newest PTF12dam data published very recently by Vreeswijk et al. (2016) show that the bolometric light curve is slightly broader, and the colour temperature is noticeably lower, reaching only 11 700 K at maximum luminosity, which may favour our P250 model.

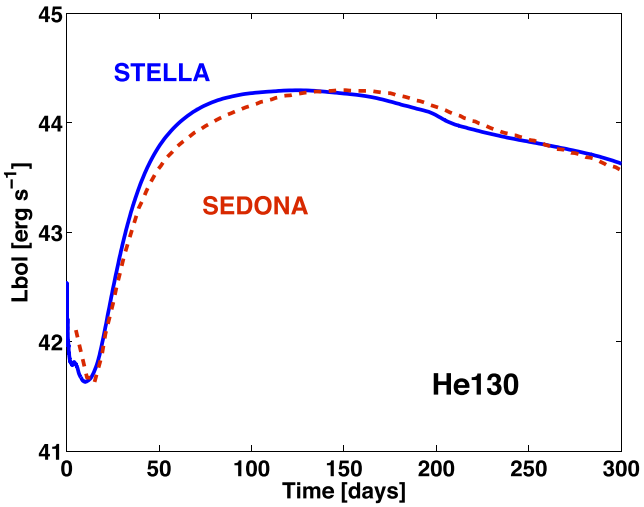

Figure 10. He130 bolometric light curves with STELLA and SEDONA codes. See the discussion in the text.

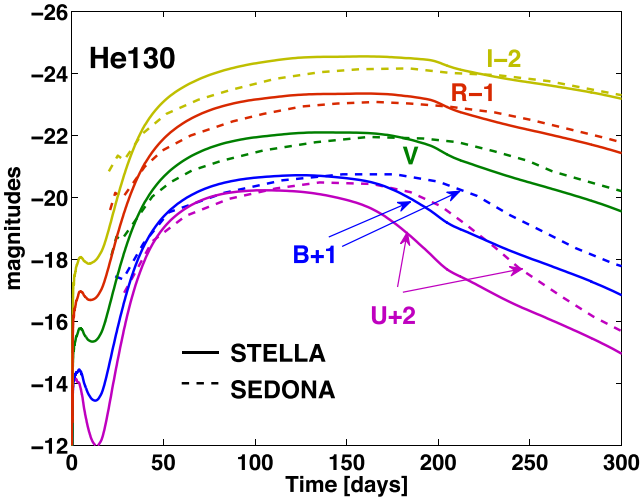

Figure 11. He130 in broad-bands with STELLA (solid) and SEDONA (dashed) codes. The light curves are, from bottom to top, *UBVRI*. *U*, *B*, *v*, *R* and *I* magnitudes are plotted with a shift of +2, +1, 0, −1, −2 mag, respectively.

In a series of additional calculations, we investigate this difference in the early light-curve evolution in more detail. In particular, we examine whether deviations from homology are causing this and to which extent details in the opacity treatment play a role in this context.

5.4 Influence of deviation from homology – nickel-bubble effect

Unlike the SEDONA version used to calculate the published light curves of the PISN model He130,[5] STELLA solves the full radiation hydrodynamical problem and is thus able to track deviation from homologous expansion. The radiation released in the radioactive decay will exert a pressure on the surrounding ejecta material as it diffuses out and will thus inflate nickel-rich regions. We now investigate the influence of this radiation hydrodynamical effect on the PISN light curve, in particular on the rise time.

For this purpose, we recalculate the He130 model with the Monte Carlo-based radiation-hydrodynamics code MCRH and determine an influence of deviation from homology on the emergent light curve analogously to Noebauer et al. (2012), where this effect has been explored in the SNe Ia context. In particular, bolometric light curves are calculated once assuming pure homologous expansion and switching of the radiation hydrodynamical coupling off and a second time with the coupling taken into account. For these MCRH calculations, a constant, frequency-independent specific interaction cross-section was adopted ($\sigma = 0.1\,\mathrm{cm^2\,g^{-1}}$). More technical details about MCRH and the simulations are provided in Appendix A. The left-hand panel of Fig. 12 shows a comparison and demonstrates that deviation from homology seems to have insignificant consequences on the emergent PISN light curve. This finding is confirmed by an additional test calculation performed with STELLA. Here, the hydrodynamical coupling has been artificially suppressed after day 1. As seen in the right-hand panel of Fig. 12, the resulting light curve is almost identical to the one obtained in the full STELLA simulation.

We emphasize that even though radiation hydrodynamical effects do not seem to play a role for calculation of bolometric light curves, the density structure is significantly modified by the dynamical effect of the radiation generated in the radioactive decay. The radiation field supplies an additional contribution to the pressure and inflates nickel-rich regions. The 'nickel-bubble effect' (well explained in Blinnikov et al. 2006; Woosley et al. 2007) develops during the first 100 d after the explosion in the He130 model as illustrated in Fig. 13. In the inner regions of the He130 model, the density is decreased relative to homologous expansion by a factor of 2 and the velocity is boosted by about 25 per cent. This dilutes the central nickel bubble and increases its radius by up to 40 per cent. Above this central region, at about 7000 km s^{-1}, a narrow shell with enhanced density is generated, containing mostly silicon, sulphur and oxygen. This phenomenon might impact the spectrum formation (see discussion in Jerkstrand et al. 2016a).

5.5 Influence of opacity

Naturally, the radiation simulations strongly depend on the underlying opacity. Therefore, we carried out additional simulations with STELLA, in which we implemented a list containing 317 700 transitions from the Kurucz & Bell (1995) data base. As illustrated in Fig. 14, the STELLA bolometric light curve computed with the extended line list tends to become more similar in shape to the SEDONA bolometric light curve. In the right-hand panel of Fig. 14, we show light curves in the *U* and *v* broad-bands for illustration. There are some differences between the light curves in the *U* band calculated with STELLA using the basic line list and the extended line list, while the light curves in the *B*, *v*, *R*, *I* bands have minor changes.

Even though the STELLA light curves obtained with the extended line list resemble the published SEDONA results more closely, there are still considerable differences. Considering the opacity treatment, the inclusion of millions of weak line transitions in an expansion opacity formalism on top of the several hundred thousand lines which are treated in detail in SEDONA may play a role here. To illustrate this, we also carried out STELLA simulations with the basic line list, in which the stronger line opacity is mimicked by fixing velocity gradient on day 10. The resulting bolometric light curve is shown as the black solid line in the left-hand panel of Fig. 14, and thick solid lines in the right-hand panel. The increased opacity

[5] Recently, Roth & Kasen (2015) have successfully developed a one-dimensional radiation hydrodynamics version of SEDONA.

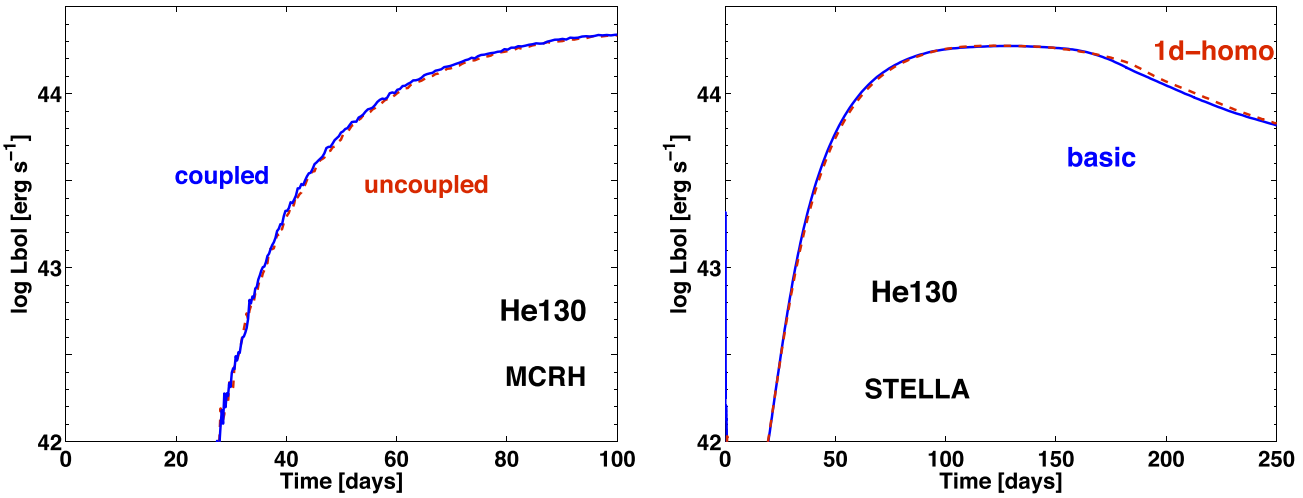

Figure 12. He130 bolometric light curves simulated with and without coupling. Left: simulations undertaken with the Monte Carlo radiation hydrodynamics code MCRH (Noebauer et al. 2012). Right: simulations undertaken with STELLA. Label '1d-homo' indicates run in which homologous expansion starts at day 1.

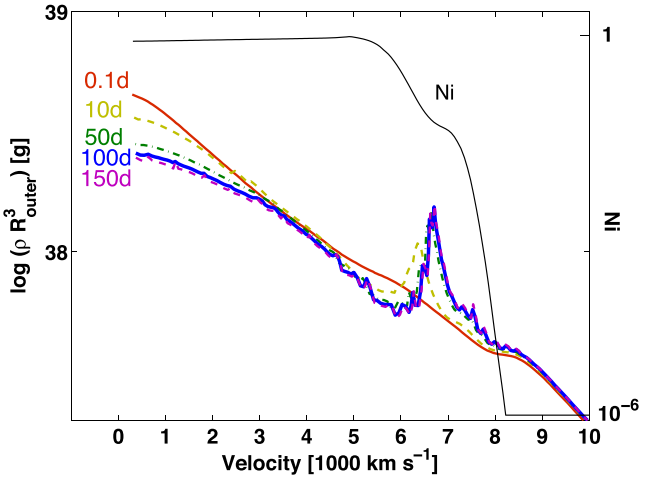

Figure 13. Scaled density–velocity evolution of the inner ejecta of the He130 model simulated with STELLA according to the nickel-bubble effect. Density is scaled to a factor of R^3_{outer}. In addition, the nickel distribution (not to scale) is shown as a thin line. See the discussion in the text.

delays the maximum and makes the light curve shallower during the re-brightening phase.

From these explorations, we conclude that the basic STELLA spectral line list contains all strong lines which govern the supernova light curve during the photospheric phase and provides quite reliable resulting bolometric light curves and magnitudes in broad-bands on the time-scale from shock breakout to several hundred days. However, the detailed shape of the light curve, from which diagnostics such as the rise time is derived, is sensitive to the details of the opacity treatment, for example to the number of line transitions taken into account.

5.6 Summary of the code comparison experiments

Based on the test calculations presented in the section, we conclude the following.

(i) When adopting the same physical assumptions, in particular when considering the idealized situation with a constant, frequency-independent specific interaction cross-section, the STELLA

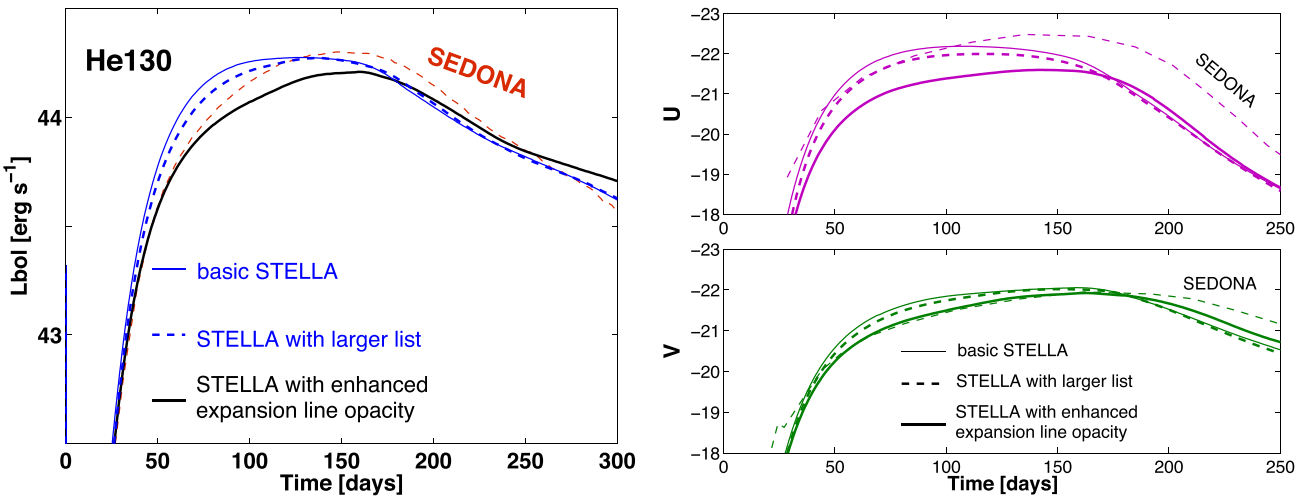

Figure 14. Bolometric (left), and U and v broad-band (right) light curve for He130 model computed with SEDONA (thin dashed), STELLA with the basic STELLA list of lines (thin solid), STELLA with the extended list of lines (thick dashed) and STELLA with the enhanced basic line opacity (thick solid).

bolometric light curve agrees very well with those computed with comparable radiative transfer and radiation hydrodynamics codes.

(ii) Since STELLA solves the coupled evolution of hydrodynamics and radiative transfer, the so-called nickel-bubble effect is seen in the STELLA calculations. This process changes the ejecta structure noticeably but has no significant effect on the bolometric light curve as various test calculations demonstrated.

(iii) The direct comparison of STELLA and SEDONA calculations seems to point to systematic differences in the rising part of the light curve. Our test calculations indicate that details of the opacity treatment seem to play an important role in this context.

6 CONCLUSIONS

In the present study, we computed the evolution, explosion and post-explosion evolution and light curves for two non-rotating stellar models with initial masses 200 $M_\odot$ (P200) and 250 $M_\odot$ (P250) at a metallicity $Z = 0.001$. For that, we consecutively used the stellar evolution code GENEC, the hydrodynamics code FLASH and the radiation hydrodynamics code STELLA. P200 and P250 lose their entire hydrogen-rich envelope due to radiatively driven winds. P200 and P250 retain only 9 and 2 $M_\odot$ of helium just before the pair-instability explosion in their outer layers. During the explosion, P200 and P250 produced 12 and 34 $M_\odot$ of radioactive nickel, thus powering luminous supernovae. P200 and P250 reach peak luminosities of 6×10^{43} and 1.4×10^{44} erg s^{-1}, respectively. The colour temperature is 8100 K (P200) and 11 000 K (P250) at the maximum light. As the photosphere resides at the bottom of oxygen shell at the peak luminosity, the P200 and P250 explosions appear as hydrogen- and helium-free (Type I) supernovae.

An important result of our study is the short rise time and fast evolution of the light curves. In particular, we find in our STELLA light-curve calculations that P200 and P250 rise to maximum in about 100 d. This finding, that light curves of PISNe models which do not retain hydrogen at the time of explosion evolve much faster than their hydrogen-rich siblings, is compatible with previous studies (Kasen et al. 2011; Dessart et al. 2013). The short rise found in our calculations is a consequence of

(i) the absence of hydrogen,
(ii) a relatively shallow helium layer and
(iii) an extended nickel distribution.

Note that we do not apply any artificial mixing in our FLASH and STELLA simulations of P200 and P250.

We examine the short rise of the STELLA light curve, by carrying out additional simulations of the helium He130 PISN model from Heger & Woosley (2002). The nickel-bubble effect has an impact on the density and velocity profiles and hydrodynamics but a negligible effect on the light-curve properties. The treatment of opacities has a noticeable impact on the light curve. Artificially enforcing a constant specific interaction cross-section enables us to obtain very similar light curves with four different codes (STELLA, MCRH, SUPERNU and V1D) for the He130 progenitor model. Increasing the number of lines in the line list included in STELLA lengthens the rise time but does not explain the full difference between STELLA and SEDONA. Nevertheless, these calculations together with the artificially enhanced line opacities demonstrate that the opacity has the strongest effect on the light-curve shape around maximum. Additionally, differences and uncertainties in the progenitor structure also affect the peak of the light curve and thus indirectly the rise time. Possibly the slope during the rise of the light curve is a more robust feature. Despite these uncertainties, we confirm that hydrogen-free PISN light curves evolve faster than those of hydrogen-rich PISNe, possibly fast enough to explain SLSNe such as PTF12dam.

We compare P200 and P250 models to the well-observed SLSN PTF12dam. From our analysis, P200 and P250 models reproduce parts of the PTF12dam data. P250 matches the earlier bolometric light curve to some degree, the peak luminosity, the colour temperature of P250 is close to the data points during 100 d after the bolometric peak, while photospheric velocity in P250 ejecta fully matches the observed velocity. P200 model better matches the late part of the light curve. To conclude, PISN scenario can still be a reasonable candidate for explaining observables of PTF12dam. The very massive (above 60 $M_\odot$) stellar origin of this event was proposed by Thöne et al. (2015) and Jerkstrand et al. (2016a), as the supernova exploded in the star-forming region of a fairly low metallicity dwarf galaxy. Other models proposed to explain PTF12dam are the magnetar-powered models (Kotera, Phinney & Olinto 2013; Nicholl et al. 2013; Metzger et al. 2014) and interaction-driven models (Chatzopoulos et al. 2013a; Baklanov et al. 2015; Chen et al. 2015; Tolstov, Nomoto & Blinnikov 2016a). The next test for our models will be to compute spectra for the photospheric phase or/and for the nebular phase. We will present the nebular spectrum simulations in the forthcoming paper (Mazzali & Kozyreva, in preparation).

ACKNOWLEDGEMENTS

The STELLA simulations were particularly carried out on the DIRAC Complexity system, operated by the University of Leicester IT Services, which forms part of the STFC DiRAC HPC Facility (www.dirac.ac.uk). This equipment is funded by BIS National E-Infrastructure capital grant ST/K000373/1 and STFC DiRAC Operations grant ST/K0003259/1. DiRAC is part of the National E-Infrastructure. AK and RH acknowledge support from EU-FP7-ERC-2012-St Grant 306901. MG and CF acknowledge support from the Department of Energy through an Early Career Award (DOE grant nno. SC0010263). The work of SB on development of the STELLA code is supported by a grant from the Russian Science Foundation (project number 14-12-00203). Work at LANL (WPE, RTW) was done under the auspices of the National Nuclear Security Administration of the US Department of Energy at Los Alamos National Laboratory under Contract No. DE-AC52-06NA25396. All LANL calculations were performed on Institutional Computing resources. UMN is supported by the Transregional Collaborative Research Centre TRR 33 'The Dark Universe' of the German Research Foundation (DFG). DRvR is supported in part at the University of Chicago by the National Science Foundation under grants AST–0909132, PHY–0822648 (JINA, Joint Institute for Nuclear Astrophysics) and PHY–1430152 (JINA-CEE, Joint Institute for Nuclear Astrophysics). AH is supported by an ARC Future Fellowship (FT120100363). AT is supported by the World Premier International Research Center Initiative (WPI Initiative, MEXT, Japan). EC is supported by Enrico Fermi Fellow. AK is grateful to Andrea Cristini for proofreading the manuscript, Stuart Sim, Markus Kromer, Stefan Taubenberger, Claes Fransson, Daniel Whalen, Luc Dessart and Daniel Kasen for fruitful discussions and useful suggestions.

REFERENCES

Abdikamalov E., Burrows A., Ott C. D., Loffler F., O'Connor E., Dolence J. C., Schnetter E., 2012, ApJ, 755, 111
Angulo C. et al., 1999, Nucl. Phys. A, 656, 3

Asplund M., Grevesse N., Sauval A. J., 2005, in Barnes T. G., III, Bash F. N., eds, ASP Conf. Ser. Vol. 336, Cosmic Abundances as Records of Stellar Evolution and Nucleosynthesis. Astron. Soc. Pac., San Francisco, p. 25
Baklanov P. V., Blinnikov S. I., Pavlyuk N. N., 2005, Astron. Lett., 31, 429
Baklanov P. V., Sorokina E. I., Blinnikov S. I., 2015, Astron. Lett., 41, 95
Baraffe I., Heger A., Woosley S. E., 2001, ApJ, 550, 890
Barkat Z., Rakavy G., Sack N., 1967, Phys. Rev. Lett., 18, 379
Bisnovatyi-Kogan G. S., Kazhdan Y. M., 1967, SvA, 10, 604
Blinnikov S. I., Bartunov O. S., 1993, A&A, 273, 106
Blinnikov S. I., Panov I. V., 1996, Astron. Lett., 22, 39
Blinnikov S. I., Dunina-Barkovskaya N. V., Nadyozhin D. K., 1996, ApJS, 106, 171
Blinnikov S. I., Eastman R., Bartunov O. S., Popolitov V. A., Woosley S. E., 1998, ApJ, 496, 454
Blinnikov S., Lundqvist P., Bartunov O., Nomoto K., Iwamoto K., 2000, ApJ, 532, 1132
Blinnikov S. I., Röpke F. K., Sorokina E. I., Gieseler M., Reinecke M., Travaglio C., Hillebrandt W., Stritzinger M., 2006, A&A, 453, 229
Bond J. R., Arnett W. D., Carr B. J., 1982, in Rees M. J., Stoneham R. J., eds, NATO ASIC Proc. 90: Supernovae: A Survey of Current Research. Reidel, Dordrecht, p. 303
Brayton R. K., Gustavson F. G., Hatchel G. D., 1972, Proc. IEEE
Carr B. J., Bond J. R., Arnett W. D., 1984, ApJ, 277, 445
Chatzopoulos E., Wheeler J. C., Vinko J., Horvath Z. L., Nagy A., 2013a, ApJ, 773, 76
Chatzopoulos E., Wheeler J. C., Couch S. M., 2013b, ApJ, 776, 129
Chatzopoulos E., van Rossum D. R., Craig W. J., Whalen D. J., Smidt J., Wiggins B., 2015, ApJ, 799, 18
Chen T.-W. et al., 2015, MNRAS, 452, 1567
Colella P., Woodward P. R., 1984, J. Comput. Phys., 54, 174
Crowther P. A., Schnurr O., Hirschi R., Yusof N., Parker R. J., Goodwin S. P., Kassim H. A., 2010, MNRAS, 408, 731
Cunha K., Hubeny I., Lanz T., 2006, ApJ, 647, L143
de Jager C., Nieuwenhuijzen H., van der Hucht K. A., 1988, A&AS, 72, 259
Densmore J. D., Urbatsch T. J., Evans T. M., Buksas M. W., 2007, J. Comput. Phys., 222, 485
Densmore J. D., Thompson K. G., Urbatsch T. J., 2012, J. Comput. Phys., 231, 6925
Dessart L., Hillier D. J., 2010, MNRAS, 405, 2141
Dessart L., Livne E., Waldman R., 2010, MNRAS, 405, 2113
Dessart L., Hillier D. J., Waldman R., Livne E., Blondin S., 2012, MNRAS, 426, L76
Dessart L., Waldman R., Livne E., Hillier D. J., Blondin S., 2013, MNRAS, 428, 3227
Dessart L., Audit E., Hillier D. J., 2015, MNRAS, 449, 4304
Dubey A., Reid L. B., Weide K., Antypas K., Ganapathy M. K., Riley K., Sheeler D., Siegal A., 2009, preprint (arXiv:0903.4875)
Eastman R. G., Pinto P. A., 1993, ApJ, 412, 731
Ekström S. et al., 2012, A&A, 537, A146
Ferguson J. W., Alexander D. R., Allard F., Barman T., Bodnarik J. G., Hauschildt P. H., Heffner-Wong A., Tamanai A., 2005, ApJ, 623, 585
Fleck J. A., Jr, Cummings J. D., 1971, J. Comput. Phys., 8, 313
Fraley G. S., 1968, Ap&SS, 2, 96
Fryxell B., Müller E., Arnett D., 1989, in Hillebrandt W., Müller E., eds, Nuclear Astrophysics.
Fryxell B. et al., 2000, ApJS, 131, 273
Gal-Yam A., 2012, Science, 337, 927
Gal-Yam A., Mazzali P. A., Manulis I., Bishop D., 2013, PASP, 125, 749
Gear C. W., 1971, Numerical Initial Value Problems in Ordinary Differential Equations. Prentice-Hall, Englewood Cliffs, NJ
Glatzel W., Kiriakidis M., 1993, MNRAS, 263, 375
Gräfener G., Hamann W.-R., 2008, A&A, 482, 945
Habibi M., Stolte A., Harfst S., 2014, A&A, 566, A6
Heger A., Woosley S. E., 2002, ApJ, 567, 532
Hirschi R., 2007, A&A, 461, 571
Hirschi R., 2015, in Vink J. S., ed., Astrophysics and Space Science Library, Vol. 412, Very Massive Stars in the Local Universe. p. 157
Humphreys R. M., Davidson K., 1994, PASP, 106, 1025
Iglesias C. A., Rogers F. J., 1996, ApJ, 464, 943
Itoh N., Adachi T., Nakagawa M., Kohyama Y., Munakata H., 1989, ApJ, 339, 354
Itoh N., Hayashi H., Nishikawa A., Kohyama Y., 1996, ApJS, 102, 411
Jerkstrand A. et al., 2016a, preprint (arXiv:1608.02994)
Jerkstrand A., Smartt S. J., Heger A., 2016b, MNRAS, 455, 3207
Kasen D., Woosley S. E., Heger A., 2011, ApJ, 734, 102
Kotera K., Phinney E. S., Olinto A. V., 2013, MNRAS, 432, 3228
Kozyreva A., Blinnikov S., Langer N., Yoon S.-C., 2014, A&A, 565, A70
Kozyreva A., Hirschi R., Blinnikov S., den Hartogh J., 2016, MNRAS, 459, L21
Kurucz R. L., Bell B., 1995, Kurucz CD-ROM. Smithsonian Astrophysical Observatory, Cambridge, MA
Lada C. J., Lada E. A., 2003, ARA&A, 41, 57
Langer N., Norman C. A., de Koter A., Vink J. S., Cantiello M., Yoon S.-C., 2007, A&A, 475, L19
Leaman J., Li W., Chornock R., Filippenko A. V., 2011, MNRAS, 412, 1419
Lee D., Deane A. E., Federrath C., 2009, in Pogorelov N. V., Audit E., Colella P., Zank G. P., eds, ASP Conf. Ser. Vol. 406, Numerical Modeling of Space Plasma Flows: ASTRONUM-2008. Astron. Soc. Pac., San Francisco, p. 243
Li W., Chornock R., Leaman J., Filippenko A. V., Poznanski D., Wang X., Ganeshalingam M., Mannucci F., 2011, MNRAS, 412, 1473
Livne E., 1993, ApJ, 412, 634
Metzger B. D., Vurm I., Hascoët R., Beloborodov A. M., 2014, MNRAS, 437, 703
Moriya T. J., 2013, PhD thesis, Univ. Tokyo, Tokyo
Moriya T., Tominaga N., Blinnikov S. I., Baklanov P. V., Sorokina E. I., 2011, MNRAS, 415, 199
Moriya T. J., Pruzhinskaya M. V., Ergon M., Blinnikov S. I., 2016, MNRAS, 455, 423
Nicholl M. et al., 2013, Nature, 502, 346
Nicholl M. et al., 2014, MNRAS, 444, 2096
Nicholl M. et al., 2015, MNRAS, 452, 3869
Noebauer U. M., Sim S. A., 2015, MNRAS, 453, 3120
Noebauer U. M., Sim S. A., Kromer M., Röpke F. K., Hillebrandt W., 2012, MNRAS, 425, 1430
Nomoto K., Thielemann F.-K., Yokoi K., 1984, ApJ, 286, 644
Nugis T., Lamers H. J. G. L. M., 2000, A&A, 360, 227
Pan T., Kasen D., Loeb A., 2012, MNRAS, 422, 2701
Phillips M. M. et al., 2007, PASP, 119, 360
Quimby R. M. et al., 2011, Nature, 474, 487
Rakavy G., Shaviv G., 1967, ApJ, 148, 803
Richardson D., Jenkins R. L., III, Wright J., Maddox L., 2014, AJ, 147, 118
Roth N., Kasen D., 2015, ApJS, 217, 9
Rydberg C.-E., Zackrisson E., Lundqvist P., Scott P., 2013, MNRAS, 429, 3658
Scannapieco E., Madau P., Woosley S., Heger A., Ferrara A., 2005, ApJ, 633, 1031
Schneider F. R. N. et al., 2014, ApJ, 780, 117
Sorokina E. I., Blinnikov S. I., Bartunov O. S., 2000, Astron. Lett., 26, 67
Sorokina E., Blinnikov S., Nomoto K., Quimby R., Tolstov A., 2016, ApJ, 829, 17
Stabrowski M. M., 1997, Simul. Modelling Pract. Theory, 5, 333
Swartz D. A., Sutherland P. G., Harkness R. P., 1995, ApJ, 446, 766
Thöne C. C., de Ugarte Postigo A., García-Benito R., Leloudas G., Schulze S., Amorín R., 2015, MNRAS, 451, L65
Timmes F. X., Swesty F. D., 2000, ApJS, 126, 501
Tolstov A. G., Nomoto K., Blinnikov S. I., 2016a, ApJ, in press
Tolstov A., Nomoto K., Tominaga N., Ishigaki M. N., Blinnikov S., Suzuki T., 2016b, ApJ, 821, 124
Verner D. A., Verner E. M., Ferland G. J., 1996, At. Data Nucl. Data Tables, 64, 1
Vink J. S., 2015, in Vink J. S., ed., Astrophysics and Space Science Library, Vol. 412, Very Massive Stars in the Local Universe. p. 77
Vink J. S., de Koter A., Lamers H. J. G. L. M., 2001, A&A, 369, 574
von Neumann J., Richtmyer R. D., 1950, J. Appl. Phys., 21, 232
Vreeswijk P. M. et al., 2016, preprint (arXiv:1609.08145)

Weaver T. A., Zimmerman G. B., Woosley S. E., 1978, ApJ, 225, 1021
Whalen D. J., Fryer C. L., Holz D. E., Heger A., Woosley S. E., Stiavelli M., Even W., Frey L. H., 2013a, ApJ, 762, L6
Whalen D. J. et al., 2013b, ApJ, 777, 110
Wollaeger R. T., van Rossum D. R., 2014, ApJS, 214, 28
Wollaeger R. T., van Rossum D. R., Graziani C., Couch S. M., Jordan G. C., IV, Lamb D. Q., Moses G. A., 2013, ApJS, 209, 36
Woodward P., Colella P., 1984, J. Comput. Phys., 54, 115
Woosley S. E., Heger A., 2015, in Vink J. S., ed., Astrophysics and Space Science Library, Vol. 412, Very Massive Stars in the Local Universe, p. 199
Woosley S. E., Heger A., Weaver T. A., 2002, Rev. Mod. Phys., 74, 1015
Woosley S. E., Kasen D., Blinnikov S., Sorokina E., 2007, ApJ, 662, 487
Yusof N. et al., 2013, MNRAS, 433, 1114
Zel'dovich Y. B., Blinnikov S. I., Shakura N. I., 1981, Physical Principles of Structure and Evolution of Stars
Zeldovich Y. B., Novikov I. D., 1971, in Thorne K. S., Arnett W. D., eds, Relativistic Astrophysics. Vol. 1: Stars and Relativity. University of Chicago Press, Chicago
Zinnecker H., Yorke H. W., 2007, ARA&A, 45, 481

APPENDIX A: DESCRIPTION OF RADIATION CODES USED FOR COMPARISON ANALYSIS

A1 MCRH

MCRH (Noebauer et al. 2012; Noebauer & Sim 2015) is a one-dimensional grey Monte Carlo (MC) radiation hydrodynamics code. Light curves for supernova ejecta are computed adopting the following assumptions:

(i) radiative equilibrium: all radiation–matter interactions are treated as pure scatterings;
(ii) radiation–matter interactions only transfer momentum but do not affect the internal energy balance;
(iii) gamma-rays generated in the nickel-56 and cobalt-56 decay are tracked in a separate MC step; their interactions with the medium are described by a grey pure absorption cross-section $\kappa = 0.03\,\mathrm{cm^2\,s^{-1}}$; Once a gamma-ray photon is absorbed, it is instantaneously converted into radiation energy (which is tracked by the main MC routine).
(iv) in contrast to the SNe Ia calculations presented by Noebauer et al. (2012), a constant radiation scattering cross-section is used (either 0.05 or $0.1\,\mathrm{cm^2\,g^{-1}}$).

The MCRH simulations are started at day 10 after the explosion. The phase prior to the starting point is treated in an analytic homologous expansion of the STELLA profile from day 1 according to the following relations:

$$r = r_0 \left(\frac{t}{t_0}\right) \quad \rho = \rho_0 \left(\frac{t}{t_0}\right)^{-3} . \tag{A1}$$

Between day 1 and day 10, the decay of nickel-56 is taken into account and the released energy is tracked. This energy, together with the initial thermal field, is used to set the radiation field at the beginning of the calculation and after accounting for adiabatic cooling losses. For the MCRH simulations, the outermost cells of the input STELLA profile are discarded (with $v > 0.1\,c$), since the high velocities in these regions are incompatible with the current design of MCRH, which only takes relativistic terms of $\mathcal{O}(v/c)$ into account. In all MCRH calculations presented here, 100 000 MC packets are used.

A2 SUPERNU

SUPERNU is a multigroup LTE radiative transfer code that employs Implicit Monte Carlo (IMC) and Discrete Diffusion Monte Carlo (DDMC; Wollaeger et al. 2013; Wollaeger & van Rossum 2014; van Rossum, in preparation). IMC solves the thermal radiative transfer equations semi-implicitly by treating some absorption and emission as instantaneous effective scattering (see, e.g., Fleck & Cummings 1971). Thus, even in purely absorbing media, MC particles can undergo isotropic scattering and wavelength redistribution. DDMC accelerates IMC over optically thick regions of space (Densmore et al. 2007) and ranges of wavelength (Abdikamalov et al. 2012; Densmore, Thompson & Urbatsch 2012) by replacing many low mean-free-path scattering events with single leakage events. SUPERNU can apply IMC and DDMC in both static and homologous, semi-relativistically expanding atmospheres. The code has been verified by analytic and semi-analytic radiative transfer tests (Wollaeger et al. 2013) and on the W7 model of SNe Ia (Nomoto, Thielemann & Yokoi 1984; Wollaeger & van Rossum 2014).

For the constant-opacity test, SUPERNU was started at day 10 with the same setup as MCRH simulations (as described in Appendix A1). For the gamma-ray transfer, SUPERNU employed a constant absorption opacity of $0.03\,\mathrm{cm^2\,g^{-1}}$ as in MCRH. The gamma-ray packets in SUPERNU are not directly converted to optical packets, but instead are used to tally the total gamma-ray energy deposition per spatial cell. The deposition energy values are then added to the thermal source for optical packets.

A3 V1D

V1D is a one-dimensional hydrodynamics version of the code VULKAN (Livne 1993). V1D solves the equations of motion using explicit Lagrangian hydrodynamics, implicitly coupled with the equations of radiative transfer. The radiative transport is solved under the approximations of LTE and grey diffusion. The grey opacities in V1D were computed based on the opacity routines of CMFGEN (Dessart & Hillier 2010; Dessart, Livne & Waldman 2010; Dessart, Audit & Hillier 2015). Hence, V1D calculates supernova ejecta evolution with coupled hydrodynamics and radiation.

This paper has been typeset from a TEX/LATEX file prepared by the author.